Applied Catalysis B: Environmental 229 (2018) 1–7

Contents lists available at ScienceDirect

Applied Catalysis B: Environmental

journal homepage: www.elsevier.com/locate/apcatb

Single-crystal TiO_2 nanorods assembly for efficient and stable cocatalyst-free photocatalytic hydrogen evolution

Yong Jiang[a], Hongyan Ning[a], Chungui Tian[a], Baojiang Jiang[a,*], Qi Li[a], Haijing Yan[a], Xuliang Zhang[a], Jianqiang Wang[b], Liqiang Jing[a], Honggang Fu[a,*]

[a] Key Laboratory of Functional Inorganic Material, Chemistry Ministry of Education of the People's Republic of China, Heilongjiang University, Harbin, 150080, China
[b] Shanghai Institute of Applied Physics, Chinese Academy of Sciences, China

ARTICLE INFO

Keywords:
TiO_2 assembly
Cocatalyst-free
Photocatalytic hydrogen evolution
Solar light

ABSTRACT

TiO_2 with abundant surface oxygen vacancies is notoriously difficult to stabilize upon photochemical oxidation, which in turn limits its photocatalytic application. To address this limitation, the gray fries cake-like TiO_2 assembly composed of single-crystal TiO_2 nanorods by in-situ carbon adherence was fabricated via hydrogenation of protonic titanate nanosheets (PTN) under normal pressure. During the hydrogenation process, the residual butyl alcohol adsorbed on PTN from tetrabutyl titanate hydrolysis can be in-situ converted into carbon in company with the formation of oxygen vacancies (O-vacancies) on TiO_2. The carbon layer and O-vacancies are able to induce the growth of single-crystal TiO_2 nanorods and their assembly to form the fries cake-like structure. Moreover, the carbon layer can not only offer a favorable reduction environment to generate rich O-vacancies on TiO_2, but also efficiently improve these O-vacancies and TiO_2 nanorods' stability during catalytic reaction. O-vacancies/carbon layer can serve as electron trap active sites which can capture and transfer electrons to improve the separation of electron-hole pairs. As a consequence, in the absence of any co-catalysts, a high efficiency of hydrogen evolution was achieved for the TiO_2 assembly with 69.7 μmol h^{-1} (quantum efficiency ~2.3% at 420 nm) under solar light irradiation. After laying six months, our TiO_2 assembly still exhibited high photocatalytic performance, which is superior to previous TiO_2-based photocatalyst. The results indicate that the photocatalytic activity of TiO_2 assembly can be enhanced by stabilizing the surface rich oxygen vacancies with carbon coating.

1. Introduction

Photocatalysis is a highly appealing technique that can convert the abundant solar energy into other types of sustainable and clean energy [1,2]. Titanium dioxide (TiO_2), a most investigated photocatalyst, has been intensively applied into water splitting, CO_2 reduction and solar cells because of its low cost, nontoxicity and good thermal stability. However, effective utilization of TiO_2 photocatalyst has been hindered by its relatively large band gap (3.2 eV) and rapid recombination of charge carriers. Many efforts have been devoted to tailor its band gap (e.g. heterogeneous element doping or point defects) and to enhance separation of photogenerated charge carriers (e.g. cocatalysts loading such as Pt and Au) [3–5]. The presence of co-catalyst can effectively decrease the activation energy, to provide more reaction active sites [6]. However, these novel metal cocatalysts are very precious and scarce. Recently, the black-colored TiO_2 with plentiful surface O-vacancies has attracted significant attention as promising visible-light photocatalyst for hydrogen evolution [7,8]. In fact, O-vacancies can also play the role of trapping photon-generated electrons as active sites of semiconductor photocatalyst, [9–13] to achieve cocatalyst-free photocatalytic activity for hydrogen evolution [14–16]. Both experimental and theoretical studies further demonstrate that O-vacancies can be also utilized to tune the band gap, and contribute to the localized electronic states and the crystal growth of TiO_2 [7,8].

Unfortunately, O-vacancies are considerably instable on surface of TiO_2 because they can be readily oxidized by air and/or water under light irradiation. Various attempts have been performed to generate more stable O-vacancies on TiO_2 by incorporating a protective carbon layer on TiO_2 via carbonization of secondary encapsulated carbon source [18–21]. In addition to increase the O-vacancies, the in-situ formed carbon layer on TiO_2 may also promote the structure of TiO_2 during growth and assembly of crystals.

Herein, we are pleased to report novel gray fries cake-like TiO_2 assemblies with in-situ formed carbon layer for cocatalyst-free

* Corresponding authors.
E-mail addresses: jiangbaojiang88@sina.com (B. Jiang), fuhg@vip.sina.com, fuhg@hlju.edu.cn (H. Fu).

https://doi.org/10.1016/j.apcatb.2018.01.079
Received 9 December 2017; Received in revised form 29 January 2018; Accepted 31 January 2018
Available online 05 February 2018
0926-3373/

photocatalytic hydrogen generation, in which single-crystal TiO_2 nanorods was developed by hydrogenation of PTN under normal pressure. The formation of carbon layer arose from the trace amount of butyl alcohol generated from the hydrolysis of tetrabutyl titanate. The presence of in-situ carbon layer created a favorable reduction environment in the assembly, to generate more O-vacancies and to increase the stability of oxygen vacancies created on the surface of TiO_2 nanorods. Using these novel gray fries cake-like TiO_2 assembly as a photocatalyst, a high photocatalytic hydrogen evolution ability (69.7 μmol h^{-1}, apparent quantum efficiency of 2.3% at 420 nm) was obtained under solar-light without any co-catalyst. Furthermore, we found that this TiO_2 assembly still exhibits high photocatalytic performance after laying six months. In order to investigate the origin of such a high photocatalytic performance, serials of experimental studies were performed.

2. Experimental procedures

2.1. Preparation of gray TiO_2 assembly

The chemical reagents were obtained from commercial reagents company without further purification. Tetrabutyl titanate (98%), Titanyl sulfate (93%) and hydrazine hydrate were purchased Sigma-Aldrich Trading Co., Ltd. The ethanol (99.7%), commercial anatase TiO_2 and P25 was obtained from Beijing Chemical Co. Ltd. In a typical synthetic procedure, 1.7 mL of tetrabutyl titanate and 10 mL of hydrazine hydrate were directly added into 75 mL ethanol. After stirring for a short time, the resulting suspension was transferred to a teflon-lined autoclave (100 mL) and heated to 150 °C for 24 h. After hydrothermal treatment, the white precipitation was washed three times using ethanol and water, respectively, and then dried under vacuum at 60 °C for 4 h to obtain white powder. Then, the as-prepared white powder was calcinated in H_2flow (gas velocity: 80 mL min^{-1}) at 400 °C–600 °C for 2 h under normal pressure conditions, with a constant heating rate of 10 °C min^{-1}. The calcination products were denoted as Hy-T, where T refers to the calcinations temperature (450 °C, 500 °C, 550 °C and 600 °C). Hy-P25 and Hy-anatase were prepared by calcinating the commercial P25-TiO_2 and commercial anatase TiO_2 under H_2 flow with same experimental condition, respectively.

2.2. Preparation of other reference samples

P25-Hy-500 was produced from P25. Firstly 0.05 g of P25 was added to a mixture solution including 20 mL of hydrazine hydrate and 60 mL of distilled water. The obtained mixture was stirred for 120 min, and then transferred to a teflon-lined autoclave (100 mL) to heat to 150 °C for 24 h. The obtained white precipitate was calcinated in H_2 flow for 2 h. The white Air-500 was obtained from protonic titanate nanosheets by same synthesis method to that of Hy-500 only under air calcination for 2 h. The Air-Hy-500 was produced from protonic titanate nanosheets by air calcination for 2 h and following H_2 thermal treatment for 2 h.

2.3. Characterization

The powder X-ray diffraction (XRD) patterns of the as-prepared products were recorded using a Rigaku D/max-IIIB diffractometer with Cu Kα radiation. Scanning electron microscopy (SEM) micrographs were taken using a Hitachi S-4800 instrument operating at 5 KV. The transmission electron microscopy (TEM) experiment was performed on JEM-2100 electron microscope (JEOL, Japan) with an acceleration voltage of 200 kV and Titan G2 60–300 (FEI) electron microscope with STEM attachment for element mapping images. Raman measurements were performed with a Jobin Yvon HR800 micro-Raman spectrometer at 457.9 nm. The Fourier transform infrared spectra (FT-IR) of the samples are collected with a PE Spectrum One B IR spectrometer. UV-vis diffuse reflectance spectra (DRS) were determined by a UV–vis spectrophotometer (Shimadzu UV-2550). X-ray Photoelectron Spectroscopy (XPS) analysis was performed on a VG ESCALAB MK II with an Mg Kα (1253.6 eV) achromatic X-ray source. The ESR spectra were collected using a JES-FA 300 spectrometer at 9.4 GHz at 300 K with 1 mW, magnetic field: 0–2 T. The surface photovoltage (SPV) measurements of the samples were carried out with a home-built apparatus. The powder samples were sandwiched between two indium-tin oxide (ITO) glass electrodes, and the change of surface potential barrier between in the presence of light and in the dark was SPV signal. The raw SPV data were normalized with a Model Zolix UOM-1S illuminometer made in China. The X-ray absorption (XAS) data at the Ti K-edge were measured at room temperature in transmission mode at beam line BL14W1 of the Shanghai Synchrotron Radiation Facility (SSRF), China. The photon energy was calibrated with Ti metal foil. Data processing was performed using the program ATHENA. The Scanning Kelvin Probe (SKP) measurements (SKP5050 system, Scotland) have been performed at normal conditions of laboratory (in ambient atmosphere). A gold electrode was used as the reference electrode. According to the calculating formula

$$W \quad \text{sample} = 5.1 - \frac{\Delta WAu}{1000} + \frac{\Delta Wsample}{1000}$$

W sample is the work function of the sample, ΔW Au is the error value calibrated by standard Au sample and ΔW sample is the measured contact potential differences of the sample. Thermogravimetric analysis was performed on a TG (TA, Q600) thermal analyzer under air with a heating rate of 10 °C/min. The hydrothermal reaction solution analytical determinations by Gas Chromatography-Mass Spectrometer (GC-MS) were performed with an Agilent 6890/5973 N system. The working parameters were injector temperature at 200 °C; interface temperature at 300 °C; carrier gas N_2 at 1 mL min^{-1}.

2.4. Photocatalytic hydrogen production measurement

The photocatalytic hydrogen production experiment was conducted in an on-line photocatalytic hydrogen production system (Au Light, Beijing, CEL-SPH$_2$N) at ambient temperature (20 °C). 20 mg catalyst was suspended in a mixture of 89 mL distilled water and 11 mL triethanolamine in the reaction cell by using a magnetic stirrer. Prior to the reaction, the mixture was deaerated to remove O_2 and CO_2 dissolved in water. An AM 1.5 solar power system (solar simulator, Oriel, USA) equipped with an AM 1.5G filter (Oriel, USA) was used as light irradiation source. Gas evolution was observed only under photoirradiation with a power density of 100 mW/cm^2, being analyzed by an on-line gas chromatograph (SP7800, TCD, molecular sieve 5 Å, N_2 carrier, Beijing Keruida Limited). The determination of the apparent quantum efficiency (AQE) for hydrogen generation was performed using same closed circulating system under illumination of a 300 W Xe lamp with optical filter (365, 420, 450, 520, and 600 nm) system. AQE was calculated under different wavelengths by the following equation:

$$AQE = \frac{2 \times \text{the number of evolved } H_2 \text{ molecules}}{\text{the number of incident photos}} \times 100\%$$

2.5. Electrochemical measurements

Photocurrent measurements were performed using a three-electrode configuration, with the typical samples films as the working electrode, saturated Ag/AgCl as the reference electrode, and platinum foil (3 × 2 cm) as the counter electrode. 1 M NaOH (pH = 13.6) purged with N_2 was used as the electrolyte. The working electrode films were prepared by doctor-blade method, using a thin glass rod to roll a paste on FTO to form a film (1 × 1 cm). The paste was prepared by stirring 0.2 g photocatalyst powders in 0.5 mL ethanol for at least 24 h. The films were annealed at 400 °C (ramp of 1 °C min^{-1}) for 1 h to make

them firm enough. An AM 1.5 solar power system was used as light irradiation source. Electrochemical impedance spectroscopy (EIS) measurements were performed in the dark and under AM 1.5 illumination in 0.5 M Na_2SO_4solution at open circuit voltage over a frequency range from 10^5 to 0.05 Hz with an AC voltage at 5 mV.

3. Results and discussions

The formation process of TiO_2 assembly obtained from titanic acid nanosheets was studied by SEM and TEM technologies. After solvothermal process, the protonic titanate nanosheet (PTN) was formed from the reaction of the tetrabutyl titanate and hydrazine hydrate (Fig. S1). It can be seen that the PTN has several micrometers with wrinkling structure. Meanwhile, GC–MS and FT-IR spectra show that a small amount of butyl alcohol from tetrabutyl titanate hydrolysis can be absorbed on PTN after the washing process (Fig. S2). The remaining butyl alcohol can be transformed into carbon under the calcination conditions. It is noted that PTN is fractionized into a great number of units and begin to form small TiO_2 crystal line after hydrogen treating at 400 °C (Figs. S3a, S4a and S4d). As the enhancement of calcination temperature to 500 °C, the size increase of TiO_2 crystalline units could be obviously observed. Its d-spacing of 0.35 nm corresponding to (101) plane of anatase TiO_2 can be observed, [22–24] which exhibit that TiO_2 crystalline begin to grow along [010] and [100] direction. Meanwhile, the sheets turn thick and crack to form nanorods but without separation, due to the carbon layer adherence (Fig. S4b,c,e and f). When reaction time rises continually, the in-situ carbon layer will restrict further growth along [010] and [100] direction, and adhere nanorods to form stable assemble structure (Fig. S4g–l). In contrast, without the protection of carbon layer, only irregular TiO_2 nanoparticles were obtained (Figs. S5 and S6), further confirming the carbon layer as structure-director in the reaction process.

The gray fries cake-like TiO_2 assembly (Hy-500) was formed by side-by-side assembly of TiO_2 nanorods under the calcination at 500 °C for 2 h (Fig. 1). It is noted that TiO_2 nanorods with diameter of 30–80 nm and lengths ranged from dozens of nanometers to 500 nm ware constituted TiO_2 assembly that of a lateral size of hundreds of nanometers (Fig. 1a and b). The high-magnification TEM image in Fig. 1c further displays a well-defined anatase TiO_2 crystalline lattice. The single crystal structure is also confirmed by selected-area electron diffraction image (inset in Fig. 1b). Interestingly, single-crystal TiO_2 nanorods are surrounded by a thin disordered layer with the thickness about 3–4 nm (Fig. 1d). In Fig. 1e, DF-STEM image and element mapping images indicate the assembly consists of Ti, O, and C elements. It is shown that C element distributes uniformly on the surface of TiO_2 nanorods, which well matches with disordered shell observed by HRTEM (Fig. 1d), suggesting the coverage of carbon layer on TiO_2.

The X-ray diffraction (XRD) and Raman measurement were conducted in order to give the information about crystal phase and composition of as-synthesized samples. Fig. S7 exhibits the typical XRD patterns of Hy-500 and Air-500 (calcinations of PTN at 500 °C for 2h under air). The diffraction peaks of both samples can be indexed to anatase phase TiO_2 (JCPDS No. 21–1272) [22–24]. The XRD patterns of reference samples from different calcination time, temperature etc. are also shown in Figs S8 and S9. Meanwhile, the FT-IR spectrum provides molecular structural information for Hy-500 and Air-500 (Fig. S10). The typical characteristic Ti-O stretches in the 475 cm^{-1} regions and the stretching vibration mode of −OH at about 3200 cm^{-1}–3600 cm^{-1} are found in Air-500 [25,26]. Interestingly, the appearance of Ti−O peaks at 491 cm^{-1} in Hy-500, with a noticeable shift toward high wave number compared with the Air-500. The shifting of characteristic peak indicates strong interactions between carbon layer and TiO_2 in the assembly structure. The thermo-gravimetric analysis shows the presence of 2% carbon in Hy-500 (Fig. S11). In Raman spectroscopy (Fig. 1f), the typical D-band (1325 cm^{-1}) and G-band (1582 cm^{-1}) are observed, proving further the presence of carbon layer in Hy-500 [27,28]. In addition, the Air-500 displays typical peaks around 141, 197, 636, 394, and 514 cm^{-1}, corresponding to the $E_{g(1)}$, $E_{g(2)}$, $E_{g(3)}$, $B_{1g(1)}$ and A_{1g} modes. Comparing with Air-500, the Hy-500 $E_{g(1)}$ peak exhibits a clear shift from 141 cm^{-1} to 153 cm^{-1}, and all peaks also show broadened band, indicate that the weakened symmetry of the TiO_2 lattice, due to the surface lattice disorder or localized defects such as O-vacancies after the hydrogen treated [29,30]. The introduction of carbon layer and rich O-vacancies possibly bring rearrangement of crystalline structure to forming TiO_2 assembly structure.

The electron spin resonance (ESR) spectra are also used to probe the oxygen vacancy signal for Hy-500 and Air-500 at room temperature (Fig. 2a). No ESR signal could be found for the Air-500 sample. In contrast, sample Hy-500 exhibits strong ESR signal at g = 1.995, which is identified as the electrons trap on high concentration oxygen vacancies [31,32]. The enhanced ESR signal implies the surface carbon layer on TiO_2 can offer more enough reduction environment favorable for the generation of rich O-vacancies. Additionally, the experimental results also show that ESR signal for O-vacancies become strong with the increase of hydrogenation treatment time and temperature due to the enough carbon layer protection (Fig. S12).

X-ray photoelectron spectra (XPS) is sensitive to the element's electronic structure [33–36]. So, the full XPS spectrum of sample is

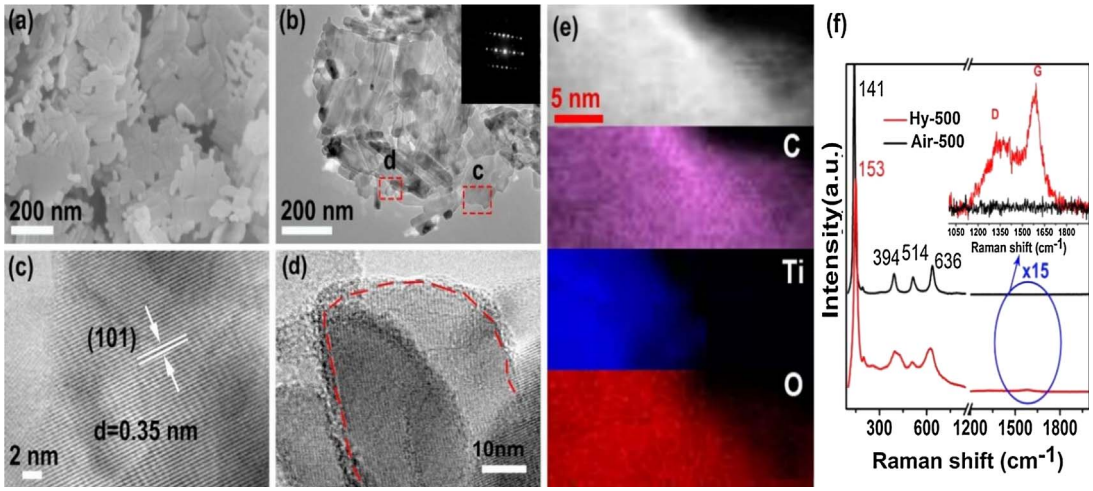

Fig. 1. The SEM image (a) and the TEM image (b) of Hy-500 obtained from titanic acid, and the inset in Fig. 1b is the SEAD of Hy-500. The HRTEM images of Hy-500 (c) and (d) correspond to red rectangular areas for Fig. 1b.(e) the DF-STEM image and element mapping images including C, Ti and O.(f) Raman spectra of Hy-500 and Air-500 (calcinations of titanic acid under air at 500 °C). (For interpretation of the references to colour in this figure legend, the reader is referred to the web version of this article).

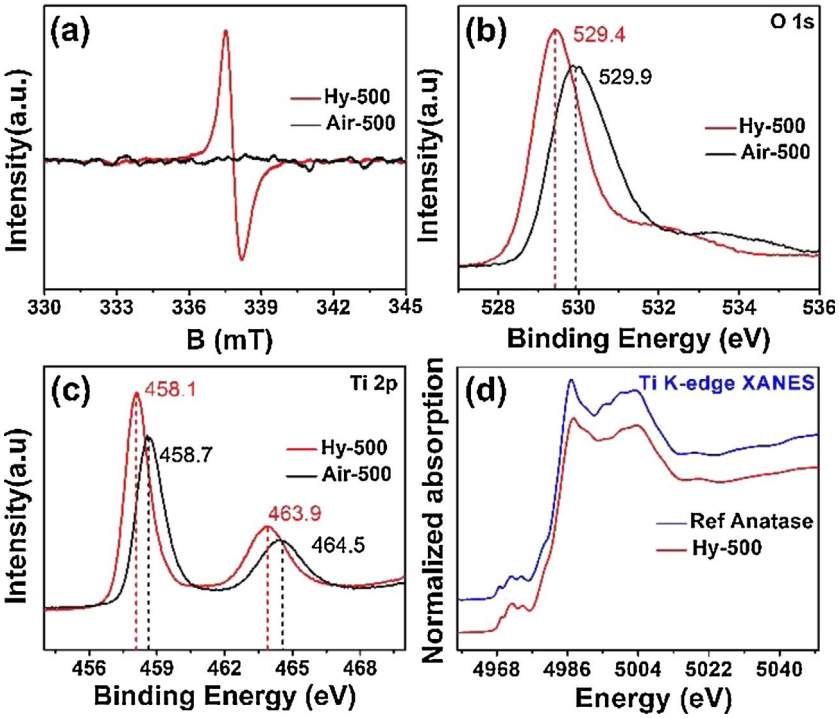

Fig. 2. The ESR spectra (a) measured at room temperature and High-resolution O1s XPS peaks (b) of Hy-500, Air-500; (c) High-resolution Ti 2p XPS spectra of Hy-500 and Air-500; (d)Ti K-edge XANES spectra for Hy-500 and reference sample.

shown as Fig. S13, showing the presence of carbon in Hy-500. The high resolution O1s XPS of Air-500 (Fig. 2b) shows the binding energies at 529.9 eV, mainly attributing to the lattice oxygen (Ti—O—Ti) of TiO_2 crystal [37–39]. However, O1 s peak of Hy-500 is slightly shifted to 529.4 eV in the comparison with that of Air-500. This downward shift is attributed to known band bending effect caused by extra electrons from O-vacancies on TiO_2 crystal lattice [40,41], which also agrees well with the ESR spectra results. In Fig. 2c, two peaks of Air-500 at 458.7 and 464.5 eV are assigned to Ti (2p3/2) and Ti (2p1/2) spin-orbital splitting photoelectrons in Ti^{4+} chemical state, respectively [17]. But the Ti2p peaks of Hy-500 slightly shift toward lower binding energy (458.1 and 463.9 eV) compared with the Air-500, which is attributed to the change of Ti chemical state within samples [42]. The above results proved the presence of oxygen deficiencies/Ti^{3+} species in the Hy-500 sample. In C1s spectra (Fig. S14), the peak at 284.9 eV is closely related to C—C bands from surface carbon layer [43,44]. The peaks at 286.3 eV and 288.2 eV are assigned to C—O bonding and C═O bonding, respectively [45]. However, the XPS technology only probes surface element chemical environment information. The X-ray absorption fine spectra (XAFS) can give whole materials structure's information. From X-ray absorption near edge absorption (XANES) for Ti K-edge of Hy-500 (Fig. 2d), no visible structure discrepancies can be found between Hy-500 and reference standard anatase TiO_2. Therefore, it is implying that O-vacancies only exist on the surface of TiO_2 which can be protected effectively by external carbon layer.

Fig. 3a is the UV–vis diffuses reflectance spectra (UV-DRS) of the samples, which clearly exhibits an absorption edge red shift from ultraviolet to visible region for Hy-500. The gray color of Hy-500 and white color of Air-500 can also be observed by optical photographs (insets in Fig. 3a), implying the presence of carbon layer for sample Hy-500. Further calculating the band gap of Hy-500 and Air-500 based on UV-DRS, the results indicate that sample band gap value is 2.98 eV and 3.21 eV for Hy-500 and Air-500, respectively. The narrow band gap exhibits the presence of carbon layer and O-vacancies can tune efficiently energy band structure of TiO_2. Fig. 3b presents XPS valence band spectra of Hy-500 and Air-500. The edge of valence band maximum energy for Hy-500 and Air-500 is 2.30 eV and 2.50 eV, respectively. The changes of valence band edge also provide sufficient evidence for the presence of defect states such as O-vacancies. Besides, reference sample TiO_2 (Air-Hy-500) only with O-vacancies, but not carbon coating was also prepared by changing calcination condition (see experimental section), and the results are shown in Figs. S15 and S16. The results further prove the carbon layer is one key factor for band engineering, growth, and assemble of TiO_2 as well as more oxygen vacancies.

The photocatalytic hydrogen production of different samples in triethanolamine/water was evaluated under AM1.5 light irradiation without addition of any co-catalyst (Fig. 4a). The proper triethanolamine/water volume ratio is also key condition for effective photocatalytic hydrogen evolution (Fig. S17), and experiments prove the maximum hydrogen production rate is obtained with triethanolamine-water volume ratio ~11/89 vol %. In the following photocatalytic measurement, no H_2 signal could be detected for Air-500. Furthermore, the reference samples Hy-P25 and Hy-anatase only show low hydrogen evolution rate (7.7 μmol h^{-1} and 2.1 μmol h^{-1}, respectively). When without carbon layer, the sample Air-Hy-500 has also shown lower hydrogen evolution rate (about 8 μmol h^{-1}). It is surprising that the average hydrogen evolution rate of Hy-500 is 69.7 μmol h^{-1}, which is about eight times higher than Hy-P25. Its photocatalytic performance is also higher than that of similar TiO_2-based photocatalyst reported when without using co-catalyst (Table S1). In addition, other samples including Hy-450, Hy-550 and Hy-600 also possess similar high photocatalytic performance. The time course of photocatalytic reaction for each sample are also shown as Fig. S18. In order to study the stability of triethanolamine during the reaction process, it is also analyzed by gas chromatography-mass spectrometry (GC-MS) before and after photocatalytic reaction, and result shows the triethanolamine is stable (Fig. S19).

Fig. 4b shows photocatalytic H_2 evolution recycled measurement using Hy-500 as the photocatalyst. Over the entire investigated time, hydrogen is produced at a steady rate without apparently decrease. Moreover, it is noted that after laying catalyst for six months, the Hy-

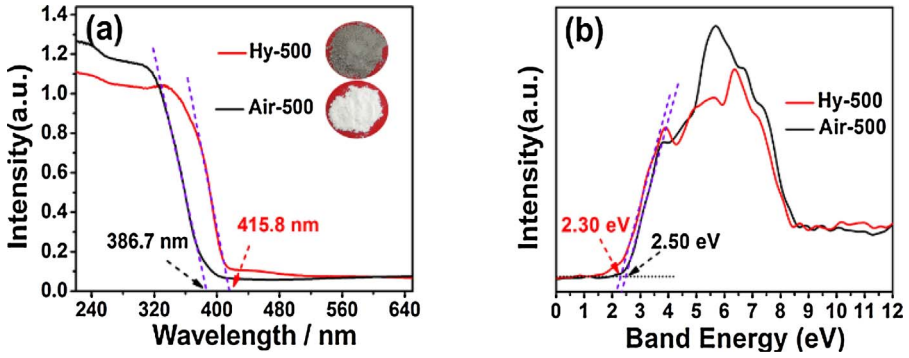

Fig. 3. (a) UV–vis diffuses reflectance spectra and (b) XPS value band spectra of Hy-500 and Air-500. (For interpretation of the references to colour in this figure legend, the reader is referred to the web version of this article).

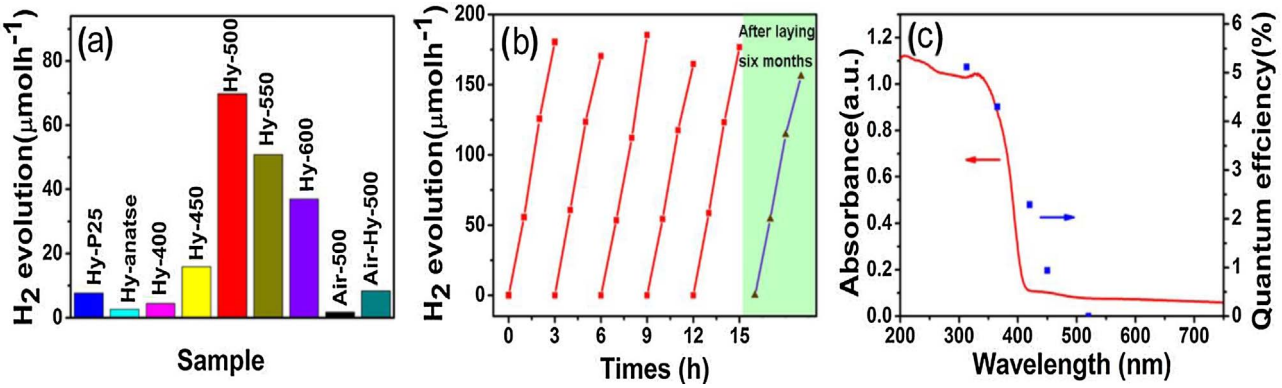

Fig. 4. (a) Photocatalytic H_2 production in triethanolamine/water (11/89 v/v) using different catalysts using AM1.5 illumination; (b) The recycled photocatalytic measurement of Hy-500 for H_2 evolution under visible light (photocatalytic measurement is also listed after laying catalyst six months); (c) Wavelength-dependent apparent quantum efficiency (AQE) of H_2 evolution over Hy-500 (right axis), UV–vis light absorption spectra of Hy-500 (left axis).

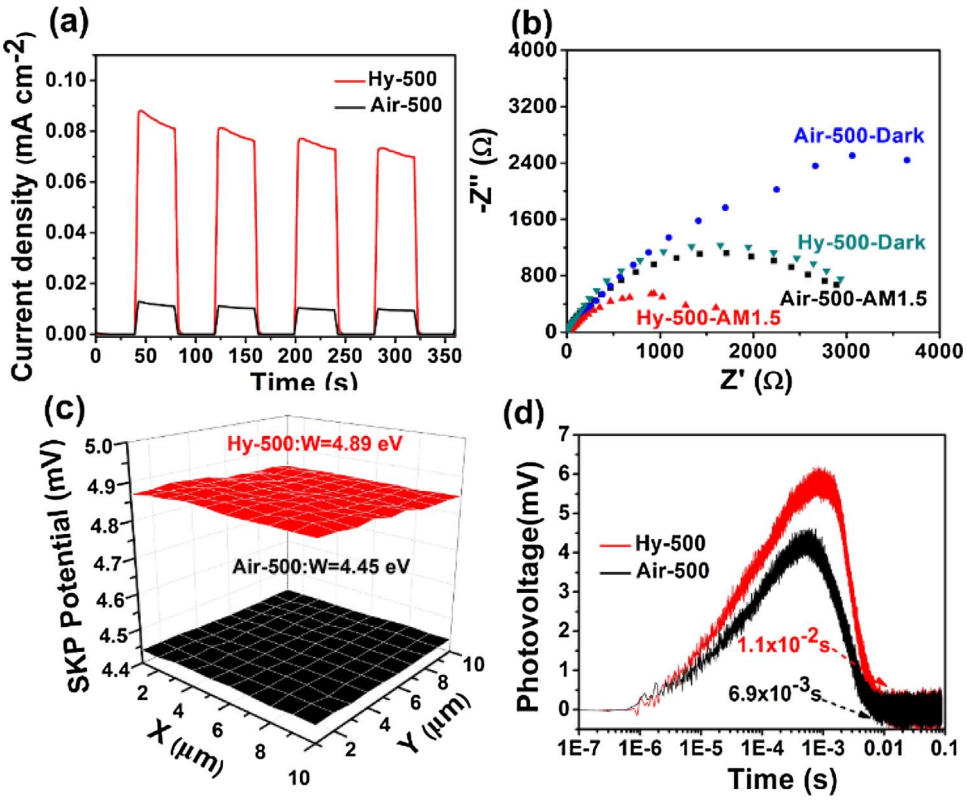

Fig. 5. (a) photoelectrochemical responses of Hy-500 and Air-500 under AM1.5 irradiation; (b) Electrochemical impedance spectroscopy (EIS) of Hy-500 and Air-500 under Dark or AM1.5 irradiation; (c) The relative work function maps of Hy-500 and Air-500; (d) Transient photovoltage spectra (TPV) responses of Hy-500 and Air-500.

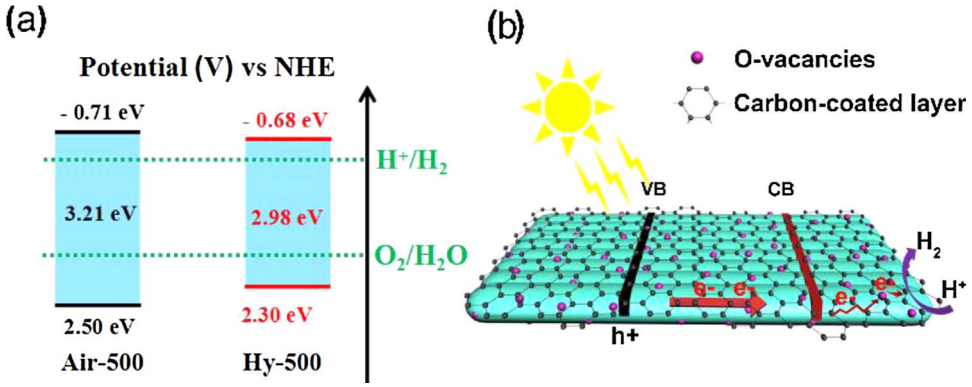

Fig. 6. (a) The energy band structure of Hy-500 and Air-500 and (b) possible transfer process of photoinduced carriers in Hy-500.

500 still shows high photocatalytic performance due to carbon protection layer (Fig. 4b). Furthermore, sample Hy-500 still keeps strong and stable O-vacancies signal after laying six months (Fig. S20). Fig. 4c gives apparent quantum efficiency (AQE) values for H_2 evolution of Hy-500 under various monochromatic light irradiations. As can be seen, variation tendency of AQE curve for Hy-500 is similar to that of UV–vis absorption spectra, and AQE value at 420 nm is about 2.3%.

In order to investigate the origin of its high photocatalytic performance without addition of any co-catalyst, serials of electrochemical studies were performed. Then the photocurrents versus time test is further performed, and the results are shown in Fig. 5a. The Hy-500 shows the higher photocurrent density, suggesting that the introduction of carbon layer and O-vacancies prompt efficiently electron-hole pairs separation. The electrochemical impedance spectroscopy also shows smaller interfacial resistance for Hy-500 electrode than that of Air-500 electrode, indicating Hy-500 electrode has better conductivity because of the presence of carbon coating (Fig. 5b).

The relative work function maps obtained from Scanning Kelvin Probe (SKP) are shown as Fig. 5c. The surface work functions (φ) of Hy-500 and Air-500 is 4.89 eV and 4.45 eV, respectively. The work function of Hy-500 is higher than that of Air-500, due to change of surface band bending and built-in electric field based on O-vacancies and carbon coating. The high work function layers could accelerate the photoelectron transfer across into the surface and then to reduce proton, [46,47] thus greatly inhibiting the electron-hole recombination and improving the photocatalytic properties.

The dynamic processes of the photogenerated charge carriers is analyzed by surface photovoltage spectra (SPV) and transient photovoltage spectra (TPV). Fig. S21 shows the SPV spectra of Hy-500 and Air-500. The Hy-500 has a stronger SPV response than that of Air-500 at 330–380 nm. It is assumed that the O-vacancies can capture and transfer photoinduced electron to carbon layer, which can restrain the recombination of electron-hole pairs and thus result in the holes' accumulation. Fig. 5d shows the transient photovoltage spectra (TPV) spectra of Hy-500 and Air-500. According to the TPV results, the Hy-500 exhibits longer lifetime (1.1×10^{-2} s) of photogenerated carriers compared with that of Air-500 (6.9×10^{-3} s) because the assembly structure with O-vacancies and carbon-coated layer greatly prolongs the lifetime of photogenerated carriers in the excited TiO_2 during photocataytic reaction procedure, which will result in high visible-light photocatalytic performance without co-catalyst.

Based on the above analyses, the possible energy band structure of Hy-500 and Air-500 can be deduced, and transfer paths of photoinduced carriers are also proposed as Fig. 6a and b. For Hy-500, the electron-hole pairs are generated under solar-light irradiation. The electron is excited to the conduction band, and then O-vacancies/carbon layer can serve as Pt-like role for active sites which can capture and transfer electrons for the reduction of proton leading to efficient hydrogen evolution. It is important that the presence of carbon layer not only control the growth and the assembly of TiO_2, but also tune prompt the stability of O-vacancies and catalyst.

4. Conclusions

In summary, gray fries cake-like assemblies composed of single-crystal TiO_2 nanorods were prepared, which have thin and stable oxygen vacancies. During the preparation process, carbon layer and O-vacancies are able to induce the growth of single-crystal TiO_2 nanorods and their assembly. Furthermore, carbon layers and O-vacancies provide high work function layer as well as active center, which will accelerate the electron-hole pairs' separation and transfer, thus greatly inhibit the electron-hole recombination and improve the photocatalytic properties. Meanwhile, carbon layers can also enhance the stability of O-vacancies and photocatalyst. This work provides a new approach to tuning morphology, electronic structure and photocatalytic performance of TiO_2 crystal.

Notes

The authors declare no competing financial interest.

Acknowledgements

We gratefully acknowledge the support of this research by the National Natural Science Foundation of China (21631004, 51372071, 21771061, 21571054). The authors thank beamline BL14W1 (Shanghai Synchrotron Radiation Facility) for providing the beam time.

Appendix A. Supplementary data

Supplementary material related to this article can be found, in the online version, at doi: https://doi.org/10.1016/j.apcatb.2018.01.079

References

[1] X.B. Chen, Sh.H. Shen, L.J. Guo, S.S. Mao, Chem. Rev. 110 (2010) 6503–6570.
[2] S.Y. Reece, J.A. Hamel, K. Sung, T.D. Jarvi, A.J. Esswein, J.J. Pijpers, D.G. Nocera, Science 334 (2011) 645–648.
[3] X.B. Chen, S.S. Mao, Chem. Rev. 107 (2007) 2891–2959.
[4] G. Liu, H.G. Yang, J. Pan, Y.Q. Yang, G.Q. Lu, H.M. Cheng, Chem. Rev. 114 (2014) 9559–9612.
[5] H. Park, H.I. Kim, G.H. Moon, W. Choi, Energy Environ. Sci. 9 (2016) 411–433.
[6] X. Chen, L. Liu, P.Y. Yu, S.S. Mao, Science 331 (2011) 746–750.
[7] J.H. Yang, D.G. Wang, H.G. Han, C. Li, Acc. Chem. Res. 46 (2013) 1900–1909.
[8] W. Zhou, W. Li, J.-Q. Wang, Y. Qu, Y. Yang, Y. Xie, K.F. Zhang, L. Wang, H.G. Fu, D.Y. Zhao, J. Am. Chem. Soc. 136 (2014) 9280–9283.
[9] J. Li, G. Zhan, Y. Yu, L.Z. Zhang, Nat. Commun. 7 (2016) 11480–11489.
[10] H. Li, J. Li, Z.H. Ai, F.L. Jia, L.Z. Zhang, Angew. Chem. Int. Ed. (2017), http://dx.doi.org/10.1002/anie.201705628.
[11] J.J. Deng, X.X. Lv, J. Gao, A.W. Pu, M. Li, X.H. Sun, J. Zhong, Energy Environ. Sci. 6 (2013) 1965–1970.
[12] N. Zhang, X. Li, H. Ye, S. Chen, H. Ju, D. Liu, Y. Lin, W. Ye, C. Wang, Q. Xu, J. Zhu,

L. Song, J. Jiang, Y. Xiong, J. Am. Chem. Soc. 138 (2016) 8928–8935.
[13] F. Lei, Y. Sun, K. Liu, S. Gao, L. Liang, B. Pan, Y. Xie, J. Am. Chem. Soc. 136 (2014) 6826–6829.
[14] N. Liu, C. Schneider, D. Freitag, U. Venkatesan, V.R. Marthala, M. Hartmann, B. Winter, E. Spiecker, A. Osvet, E.M. Zolnhofer, K. Meyer, T. Nakajima, X. Zhou, P. Schmuki, Angew. Chem. Int. Ed. 53 (2014) 14201–14205.
[15] N. Liu, C. Schneider, D. Freitag, M. Hartmann, U. Venkatesan, J. Muller, E. Spiecker, P. Schmuki, Nano Lett. 14 (2014) 3309–3313.
[16] N. Liu, V. Haublein, X. Zhou, U. Venkatesan, M. Hartmann, M. Mackovic, T. Nakajima, E. Spiecker, A. Osvet, L. Frey, P. Schmuki, Nano Lett. 15 (2015) 6815–6820.
[17] Q. Zhu, Y. Peng, L. Lin, C.M. Fan, G.Q. Gao, R.X. Wang, J. Mater. Chem. A 2 (2014) 4429–4437.
[18] R. Boppella, J.-E. Lee, F.M. Mota, J.Y. Kim, Z. Feng, D.H. Kim, J. Mater. Chem. A. 5 (2017) 7072–7080.
[19] B. Jiang, Y. Tang, Y. Qu, J.Q. Wang, Y. Xie, C. Tian, W. Zhou, H. Fu, Nanoscale 7 (2015) 5035–5045.
[20] G. Fu, P. Zhou, M. Zhao, W. Zhu, S. Yan, T. Yu, Z. Zou, Dalton Trans. 44 (2015) 12812–12817.
[21] B. Li, Z. Zhao, F. Gao, X. Wang, J. Qiu, Appl. Catal. B 147 (2014) 958–964.
[22] J. Pan, G. Liu, G.Q. Lu, H.M. Cheng, Angew. Chem. Int. Ed. 50 (2011) 2133–2137.
[23] R.G. Li, Y.X. Weng, X. Zhou, X.L. Wang, Y. Mi, R.F. Chong, H.X. Han, C. Li, Energy Environ. Sci. 8 (2015) 2377–2382.
[24] H. Lin, L. Li, M. Zhao, X. Huang, X. Chen, G. Li, R. Yu, J. Am. Chem. Soc. 134 (2012) 8328–8331.
[25] H. Zhang, X.J. Lv, Y.M. Li, Y. Wang, J.H. Li, ACS Nano 4 (2010) 380–386.
[26] K.S. Liu, H.G. Fu, K.Y. Shi, F.S. Xiao, L.Q. Jing, B.F. Xin, J. Phys. Chem. B 109 (2005) 18719.
[27] B. Zhao, F. Chen, W. Qu, J. Zhang, Chem. Asian J. 5 (2010) 1546–1549.
[28] B.J. Jiang, C.G. Tian, W. Zhou, J.Q. Wang, H.G. Fu, Chem. Eur. J. 17 (2011) 8379–18722.
[29] A.C. Ferrari, J. Robertson, Phys. Rev. B 61 (2000) 14095–14107.
[30] K.T. Lee, X. Ji, M. Rault, L.F. Nazar, Angew. Chem. Int. Ed. 4 (2009) 5661–5665.
[31] A. Naldoni, M. Allieta, S. Santangelo, M. Marelli, F. Fabbri, S. Cappelli, C.L. Bianchi, R. Psaro, V. Dal Santo, J. Am. Chem. Soc. 134 (2012) 7600–7603.
[32] T. Xia, C. Zhang, N.A. Oyler, X. Chen, Adv. Mater. 25 (2013) 6905–6910.
[33] H.W. Huang, X.W. Li, J.J. Wang, F. Dong, P.K. Chu, T.R. Zhang, Y.H. Zhang, ACS Catal. 5 (2015) 4094–4103.
[34] H.W. Huang, Sh.Ch. Tu, Ch. Zeng, T.R. Zhang, Ali H. Reshak, Y.H. Zhang, Angew. Chem. Int. Ed. 56 (2017) 11860–11864.
[35] H.W. Huang, R.R. Cao, Shixin Yu, Kang Xu, Weichang Hao, Yonggang Wang, Fan Dong, Tierui Zhang, Yihe Zhang, Appl. Catal. B Environ. 219 (2017) 526–537.
[36] H.W. Huang, Ke. Xiao, T.R. Zhang, F. Dong, Y.H. Zhang, Appl. Catal. B Environ. 203 (2017) 879–888.
[37] B.J. Jiang, C.G. Tian, Q.J. Pan, Z. Jiang, J.Q. Wang, W.S. Yan, H.G. Fu, J. Phys. Chem. C 115 (2011) 23718–23725.
[38] S.M. Prokes, J.L. Gole, X. Chen, C. Burda, W.E. Carlos, Adv. Funct. Mater. 15 (2005) 161–167.
[39] I.R. Macdonald, S. Rhydderch, E. Holt, N. Grant, J.M.D. Storey, R.F. Howe, Catal. Today 182 (2012) 39–45.
[40] Z. Wang, C. Yang, T. Lin, H. Yin, P. Chen, D. Wan, F. Xu, F. Huang, J. Lin, X. Xie, M. Jiang, Energy Environ. Sci. 6 (2013) 3007–3014.
[41] G. Ketteler, S. Yamamoto, H. Bluhm, K. Andersson, D.E. Starr, D.F. Ogletree, H. Ogasawara, A. Nilsson, M. Salmeron, J. Phys. Chem. C. 111 (2007) 8278–8282.
[42] A. Sinhamahapatra, J.P. Jeon, J.S. Yu, Energy Environ. Sci. 8 (2015) 3539–3544.
[43] S.I. Nikitenko, T. Chave, C. Cau, H.-P. Brau, V. Flaud, ACS Catal. 5 (2015) 4790–4795.
[44] R. Ren, Z. Wen, S. Cui, Y. Hou, X. Guo, J. Chen, Sci. Rep. 5 (2015) 10714–10725.
[45] P.C. Angelome, L. Andrini, M.E. Calvo, F.G. Requejo, S.A. Bilmes, G.J.A.A. Soler-Illia, J. Phys. Chem. C 111 (2007) 10886–10893.
[46] S.U. Nanayakkara, G. Cohen, C.S. Jiang, M.J. Romero, K. Maturova, M.Al. Jassim, J. Lagemaat, Y. Rosenwaks, J.M. Luther, Nano Lett. 13 (2013) 1278–1284.
[47] X. Zhang, Y. Lin, D. He, J. Zhang, Z. Fan, T. Xie, Chem. Phys. Lett. 504 (2011) 71–75.